Matter and Radiation at Extremes

RESEARCH ARTICLE | MAY 21 2026

# Cascaded ion emissions from copper plasma produced by an X-ray free-electron laser

T. Burian ; J. Krása ; M. Šmíd ; M. Krupka ; M. Stránský ; Z. Jurek ; R. Santra ; J. Chalupský ; L. Vyšín ; A. Horynová ; J. Bulička ; Š. Jelínek ; M. Kozlová ; M. Mašek ; O. Humphries ; C. Baehtz ; V. Bouffetier ; E. Brambrink ; V. Cerantola ; T. E. Cowan ; V. Hájková ; J. Kaa ; Z. Konôpková ; M. Makita ; X. Pan ; T. R. Preston ; J.-P. Schwinkendorf ; A. Schropp ; R. Štefaníková ; W. Wang ; U. Zastrau ; K. Falk ; L. Juha

Check for updates

*Matter Radiat. Extremes* 11, 057601 (2026)
https://doi.org/10.1063/5.0314214

View Online
Export Citation

22 May 2026 09:11:48

AIP Publishing

Matter and Radiation at Extremes

RESEARCH ARTICLE

pubs.aip.org/aip/mre

# Cascaded ion emissions from copper plasma produced by an X-ray free-electron laser

Cite as: Matter Radiat. Extremes 11, 057601 (2026); doi: 10.1063/5.0314214
Submitted: 27 November 2025 • Accepted: 5 May 2026 •
Published Online: 21 May 2026

View Online Export Citation CrossMark

T. Burian,[1] J. Krása,[1,a)] M. Šmíd,[2] M. Krupka,[1,3] M. Stránský,[1] Z. Jurek,[4] R. Santra,[4,5] J. Chalupský,[1] L. Vyšín,[1] A. Horynová,[1,6] J. Bulička,[1,7] Š. Jelínek,[1,3,7] M. Kozlová,[3,8] M. Mašek,[1] O. Humphries,[9] C. Baehtz,[2,9] V. Bouffetier,[2] E. Brambrink,[9] V. Cerantola,[10] T. E. Cowan,[2] V. Hájková,[1] J. Kaa,[11] Z. Konôpková,[9] M. Makita,[9] X. Pan,[2] T. R. Preston,[9] J.-P. Schwinkendorf,[2] A. Schropp,[12] R. Štefaníková,[2,13] W. Wang,[9,12] U. Zastrau,[9] K. Falk,[1,2] and L. Juha[1]

## AFFILIATIONS

[1]Department of Radiation and Chemical Physics, Institute of Physics, Czech Academy of Sciences, Na Slovance 2, 18200 Prague 8, Czech Republic
[2]Institute of Radiation Physics, Helmholtz-Zentrum Dresden-Rossendorf (HZDR), Bautzner Landstraße 400, 01328 Dresden, Germany
[3]Laser Plasma Department, Institute of Plasma Physics, Czech Academy of Sciences, Za Slovankou 3, 18200 Prague 8, Czech Republic
[4]Center for Free-Electron Laser Science CFEL, Deutsches Elektronen-Synchrotron DESY, Notkestraße 85, 22607 Hamburg, Germany
[5]Department of Physics, University of Hamburg, Notkestraße 9-11, 22607 Hamburg, Germany
[6]Department of Nuclear Chemistry, Faculty of Nuclear Science and Physical Engineering, Czech Technical University in Prague, Břehová 7, 11519 Prague 1, Czech Republic
[7]Department of Surface and Plasma Science, Faculty of Mathematics and Physics, Charles University, V Holešovičkách 2, 18200 Prague 8, Czech Republic
[8]The Extreme Light Infrastructure ERIC, ELI Beamlines Facility, Za Radnicí 835, 25241 Dolní Břežany, Czech Republic
[9]European XFEL, Holzkoppel 4, 22869 Schenefeld, Germany
[10]Department of Earth and Environmental Sciences, University of Milano-Bicocca, Piazza dell'Ateneo Nuovo 1, 20126 Milan, Italy
[11]Carl Zeiss SMT GmbH, Rudolf-Eber-Straße 2, 73447 Oberkochen, Germany
[12]Centre for X-Ray and Nano Science CXNS, Deutsches Elektronen-Synchrotron DESY, Notkestraße 85, 22607 Hamburg, Germany
[13]TUD Dresden University of Technology, 01062 Dresden, Germany

[a)]**Author to whom correspondence should be addressed:** krasa@fzu.cz

## ABSTRACT

Ultrafast, high-power lasers operating in the near-infrared (NIR) region are key to accelerating ions to extremely high energies. By changing the laser wavelength from the NIR region to the hard X-ray range, the photon energy increases more than 10 000 times. The interaction mechanisms and, consequently, radiation attenuation lengths differ significantly between these two spectral ranges. Here we report the use of an X-ray free-electron laser (European XFEL, Germany) delivering 9.3 keV photons in 25 fs pulses and a total energy of 0.35 mJ on a solid target. Electrons and ions escaping from an irradiated 3 $\mu$m Cu foil into vacuum were investigated by a time-of-flight technique using windowless electron multipliers that enable the measurement of very weak currents. A model based on a shifted Maxwell–Boltzmann velocity distribution of species was used to analyze the detector signals. The method used made it possible to determine the temperatures of hot electrons and protons, their center-of-mass energy, the charge states of the isotopes $^{63}$Cu and $^{65}$Cu, and the magnitude of the voltage arising in the double layer that accelerated them, and to estimate the repetition frequency of their cascade emission from the plasma. Computer simulations revealed the evolution of the electron density and temperature, the ion charge state distribution, and the time scales of processes

22 May 2026 09:11:48


© Author(s) 2026

occurring in the bulk of irradiated matter. Good correlation of theoretical and experimental results over the range of high-energy-density states demonstrates the capability to provide critical data to develop plasma models in the warm dense matter regime.

© 2026 Author(s). All article content, except where otherwise noted, is licensed under a Creative Commons Attribution (CC BY) license (https://creativecommons.org/licenses/by/4.0/). https://doi.org/10.1063/5.0314214

## I. INTRODUCTION

Ion emission from plasmas occurs in a wide range of systems generated by high-power laser interactions, making it possible to address various questions that arise in the fundamental physics of hot dense plasma and warm dense matter using ion diagnostics.[1–3] There is strong motivation for the study of ion emissions[4–8] from dense plasmas, since these are of practical importance in the field of inertial confinement fusion (ICF) science and technology. Detailed knowledge of ion emission is needed for the reliable design of prospective inertial fusion energy (IFE) reactors, because their first walls are exposed not only to neutrons and photons, but also to charged particles released from burning nuclear fuel. The development and design of laser ion sources for ion accelerators[4–8] represents another motivation. Ion emission from plasmas will also be of practical importance in laboratory or industrial applications of compact repetitive extreme ultraviolet (EUV)/X-ray free-electron lasers (FELs), although, in spite of definite progress in the development of compact FEL devices,[9–12] these are not yet widely available. Ions emitted from the XUV/X-ray laser-irradiated surfaces of solid samples can be also used for chemical analysis, assessment of radiation resistance, and elemental composition imaging (see, e.g., Refs. 13–16).

This work aims to identify the dynamic processes responsible for the characteristic properties of ion emission from a dense plasma created by heating a copper foil with ultrashort intense radiation from an X-ray FEL. Since the critical density values calculated for X-ray irradiation exceed the density of electrons in solids, focused short-wavelength laser beams produce a solid-density plasma through volumetric heating of target material (see, e.g., Refs. 17–19). Depending on the intensity and the attenuation length of short-wavelength radiation, this is either warm dense matter[17,18] or hot dense plasma.[19] The boundary between these is not sharply determined; it is defined by convention and varies across different subfields of plasma physics and high-energy-density physics. Ion emission from plasmas produced by ultrafast X-ray laser beams has been studied in the soft X-ray spectral range only. The irradiation conditions achieved in the present study differ significantly from those in experiments performed at the FLASH and FLASH2 soft X-ray FELs,[20–22] primarily because of the entirely different attenuation length of X-ray laser radiation in the irradiated material and the ability of hard X-rays to ionize electrons from inner shells.

## II. EXPERIMENTAL ARRANGEMENT

The experiment was performed using the High Energy Density (HED) Scientific Instrument at the European XFEL facility.[23–25] The XFEL beam generated in the SASE regime was focused by a stack of 20 beryllium lenses (with radius of curvature 50 $\mu$m) with a focal length of 30–40 cm in the range of XFEL photon energies from 8750 to 9900 eV with a 25 eV bandwidth. This experimental study concerns ion emission from a 3 $\mu$m thin Cu foil exposed to the focused X-ray beam with an energy of 9.3 keV and an approximately Gaussian spot with a diameter of 0.4 $\mu$m. The damage pattern (beam imprint in a $PbI_2$ layer on a CVD diamond substrate[26]) characteristics were obtained by means of Nomarski (differential interference contrast, DIC) microscopy. The application of the beam imprinting technique has been described in detail elsewhere.[27] The target consisted of a single Cu foil fixed in a frame with a $6 \times 30$ mm$^2$ window, allowing continuous exposure at a repetition rate of 10 Hz, where the speed of the target holder was adjusted to maintain a crater (imprint) spacing of 20 $\mu$m. The ions were produced by 25 fs X-ray pulses irradiating the target surface with an average pulse energy of 0.35 mJ, corresponding to a fluence of $\approx 2.8 \times 10^5$ J·cm$^{-2}$ ($I\lambda^2 \approx 2 \times 10^{17}$ W·cm$^{-2}$·$\mu$m$^2$).

The energy of the pulse hitting the target was measured by a photodiode connected to a diamond diaphragm placed between the last element of the focusing optics and the target.[25] This detector has been absolutely calibrated with X-ray photoionization gas monitors. The last lens set had an effective aperture of 300 $\mu$m, which was overfilled using a beam size of ~350–500 $\mu$m, ensuring that the full aperture was illuminated, and to mitigate fluctuations due to pointing instability. Each data run typically consisted of several thousand shots with nominally identical conditions. Owing to the high sensitivity of the energy distribution of the emitted ions to SASE-FEL pulse energy fluctuations, pulses were not averaged, but analyzed individually, shot-by-shot. The ion emission was measured without any change in focus position with respect to the target surface to obtain a dataset characterizing shot-to-shot variation in ion emission, highlighting the details of the ion emission mechanism responding to fluctuations in laser–target interactions.

Owing to the low number of ions expected to be liberated from the target for the given interaction conditions, ion signals were registered by an open electron multiplier (EM) type 119EM, which is an ultrasensitive detector of charged particles. This windowless EM equipped with Be–Cu dynodes was manufactured by Thorn EMI Electron Tubes, UK. It has a Venetian blind structure, consisting of a ten-slat entrance dynode (2.16 cm-diameter aperture), followed by a system of 17 dynodes. The initial amplification of electron current certified by the manufacturer was $6.26 \times 10^6$ with an operating potential of −3 kV applied to the first dynode, while the input grid was grounded. The detector rise time was ≈1 ns. Calibration of electron multipliers is needed for ion detection because the ion-induced emission of electrons from the first dynode depends not only on the quality of a dynode's surface, but also on the intercepted ion species and their energy. The calibration has shown a dependence of the EM gain mainly on the charge state of detected ions, with a weaker dependence on the impact velocity. Since we were unable to calibrate the gain of the open electron multiplier during this experiment, we used previous data[28] for the range of low ion kinetic energies encountered in our experiment to determine the value of this gain as $5 \times 10^5$.

22 May 2026 09:11:48


© Author(s) 2026

The EM detector was placed in front of the target, on whose front side the X-ray beam was incident along its normal. The distance of the EM from the interaction point was 920 mm, with horizontal and vertical angles of 8° and 9.5°, respectively, to the direction of laser beam propagation. Another EM was also used in the experiment to detect ions emitted from the back of the target, but its signal was mostly below the detection threshold.

## III. THEORETICAL DESCRIPTION

### A. Modelling of material properties of copper irradiated by XFEL pulses

For more than a decade, experiments and numerical simulations of processes in hot dense matter produced by ultrashort XFEL pulses have been ongoing. This research covers various thematic areas such as spectroscopic characterization of fixed-density plasmas, various transport mechanisms, such an energy transport, charged-particle, and radiation transport, evaluations of collision rates in solid-density plasmas, and plasma screening.[29–32] To gain insight into the dynamics of XFEL-irradiated copper, we performed simulations with XMDYN.[33,34] XMDYN describes the high-intensity X-ray-driven time evolution of matter. It is a hybrid approach combining Monte Carlo (MC) and molecular dynamics (MD) techniques based on parameters calculated from first principles. In XMDYN, bound electrons are assumed to belong to specific atomic orbitals, and so the instantaneous electronic structure may be described via the occupation number of the orbitals. During irradiation, various inner-shell processes (photoionization and Auger–Meitner and fluorescent decays) are considered via an MC algorithm, fed with atomic parameters provided by the *ab initio* tool XATOM.[33,35–37] At an ionization event, beside the change of the relevant occupation numbers, a free electron leaves the parent ion, represented by a classical particle in the model. From the perspective of real-space dynamics, atoms and atomic ions are also handled as classical particles. MD is used to track the motion of these particles, considering the Coulomb forces among the charges.

Capturing the dynamics of a copper foil of macroscopic dimensions is still not computationally feasible using the microscopic description provided by XMDYN, especially on macroscopic time scales. Therefore, we chose to simulate the early ionization characteristics of Cu bulk-irradiated by an XFEL pulse with a photon energy of 9.3 keV and a Gaussian temporal intensity envelope (25 fs FWHM). The bulk is simulated using a periodic 4 × 4 × 4 FCC supercell with 256 copper atoms starting with zero velocities (0 K initial state). Three XMDYN trajectories per fluence already led to results with acceptable statistics. Each such trajectory corresponds to a specific realization of the time evolution of all particles and electronic configurations within the supercell. The data presented in the following are the average of the three XMDYN trajectories computed.

The resulting time evolution of the relative abundance of $Cu^{q+}$ ions with charge state, $q$, ranging from 1 to 22, is shown in Fig. 1(a). Multiply charged Cu ions are produced in the early period of the laser pulse interaction with the Cu foil. About 10 fs before the peak of the XFEL pulse, they disappear owing to progressive ionization. After the end of the laser interaction, highly charged $Cu^{q+}$ ions with $q$ = 20 or 21 dominate. The number of ions carrying a charge state higher than 22 is negligible. Their gradual recombination after

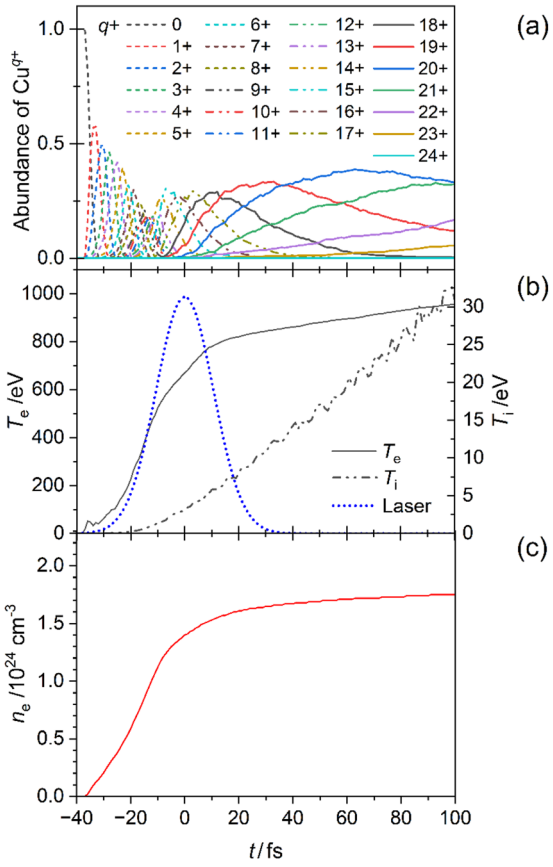


**FIG. 1.** Dynamical properties of bulk Cu irradiated by an intense XFEL pulse, as extracted from XMDYN simulations. The X-ray pulse parameters assumed are given in the text. (a) Time evolution of the relative abundance of $Cu^{q+}$ ions, where $q$ varies from 1 to 24. The 0 label indicates the relative abundance of neutral atoms. (b) Time evolution of electron and ion kinetic temperatures (i.e., mean kinetic energies) $T_e$ and $T_i$, respectively. (c) Electron density of Cu plasma. The laser intensity is in arbitrary units.

100 fs with respect to the peak of the pulse was not simulated. The simulation of the plasma evolution details the time dependences of the electron and ion kinetic temperatures (average kinetic energies) from the simulations are shown in Fig. 1(b) and that of the electron density is shown in Fig. 1(c). Note that the ions are still far from equilibrium on such a short time scale.

Our calculations revealed only a weak dependence of the ionization processes on fluence, as shown in Fig. 2 for values of 198, 398, 796, 1194, and 1591 kJ·cm$^{-2}$. While the fluence increased almost eight times, the number of primary photoionization events in the simulation time window increased only 2.4 times, since the intensity conditions were sufficient for saturable absorption effects,[35] with the resulting Auger decay channel stagnating for fluences greater than 800 kJ·cm$^{-2}$. The total number of collisional ionization events showed no relevant fluence dependence. We note that in the experiment, the target was irradiated with a spatially nonuniform fluence distribution, owing to the focusing properties of the beam.[38,39] Therefore, the measured signal does not correspond to a

22 May 2026 09:11:48


© Author(s) 2026

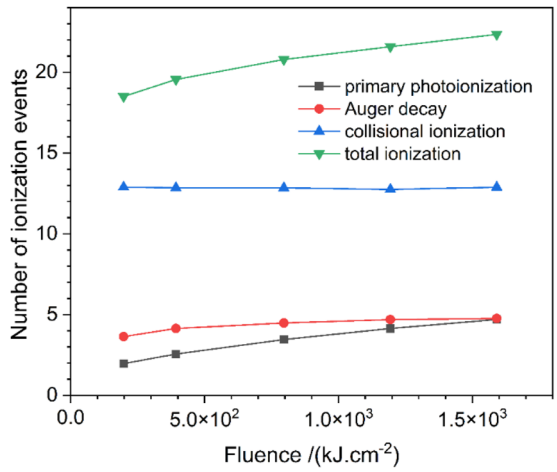


**FIG. 2.** Fluence dependence of the dominant ionization processes initiated by a 25 fs XFEL pulse with a photon energy of 9.3 keV: number of ionization events per atom within the simulation time window.

fixed fluence value, but contains contributions from volumes excited at different fluence values from zero up to the maximum in the center of the focus. We do not consider in our theoretical demonstration such volume integration effects.

### B. Double-layer structure on the plasma surface

The interaction of the XFEL pulse with the Cu foil leads to the formation of a highly ionized plasma, as shown in the simulations presented above. Another process is the expansion of plasma from the focus of the laser beam on the front surface of the target into a vacuum. In this context, we must also consider the basic phenomena and physical processes associated with the expansion of plasma into a vacuum, which have been studied for a long time both theoretically and experimentally in experiments with infrared (IR) to ultraviolet (UV) lasers. The fundamental difference between plasma produced in a target and plasma expanding into a vacuum is that a bulk plasma can be considered to be homogeneous, while an expanding plasma is very inhomogeneous. It is known that during the expansion, a new process emerges that can accelerate ions to energies significantly higher than their thermal energy.[40] As a plasma expands into a vacuum, it becomes rarefied. The fastest (hot) electrons from the energy tail of the energy distribution escape from the plasma surface, leaving behind slower positively charged ions establishing a double layer (DL) of thickness of the Debye length with an internal electric field.[40] This electric field is a function of time, and the structure of the DL is changing in time and space. The static electric field $E$, related to the potential $\phi$, satisfies Poisson's equation based on the local difference in electron $n_e$ and ion $n_i$ densities:

$$\frac{\partial E}{\partial z} = -\frac{\partial^2 \phi}{\partial z^2} = -4\pi e(n_e - \bar{q} n_i), \tag{1}$$

where $z$ is the target's surface-normal coordinate, $e$ is the electron charge, and $\bar{q}$ is the average degree of ionization.

Many theoretical models of the DL at the periphery of various plasmas found in a variety of laboratory plasmas have been published.[40–42] However, in the case of a laser-produced plasma, two- and three-dimensional models should include more moving DLs resulting from charged particle drift and mismatches at the plasma boundary. Because a monotonic potential step or a series of steps and dips formed by DLs accelerates ions to high energies, even in the post-interaction phase, the models are complex and differ from each other depending on the type of plasma. Since, to our knowledge, the expanding plasma produced by hard X rays has not been investigated, a theoretical model is not available. However, information about the expansion of a laser-produced plasma is available from experiments with pulsed IR to UV lasers, which are used in this work to characterize ion emission induced by XFEL pulses. The presented analysis of ion emission from copper foil irradiated by XFEL pulses could provide information for a future model of expanding inhomogeneous plasmas.

## IV. EXPERIMENTAL RESULTS AND DISCUSSION

### A. Shot-to-shot fluctuations

The properties of the plasma produced by a laser pulse generally exhibit shot-to-shot fluctuations in the signals of the detectors used. These fluctuations are attributed both to the transient evolution of the plasma, which is inhomogeneous and anisotropic, and to the possible influence of the imperfect structure of the surface of the foil target (caused, for example, by cracks and ripples) on the plasma production. As a first step, it is desirable to consider the influence of shot-to-shot variations in the absolute photon flux on the outcome of the interaction process, as shown in Fig. 9 of Ref. 23, where single-pulse spectra recorded by a HED-flex spectrometer at 6 keV show noteworthy shot-to-shot fluctuations. This is a consequence of the fact that the interaction of the X-ray laser with the target triggers dynamic effects in the plasma, such as isochoric heating and ionization, generation of extreme fields and hydrodynamic oscillations, radiation sources, and warm/hot dense plasmas. After the interaction, shock wave generation, thermal diffusion, magnetic Z-pinch-induced and thermal pressure-induced compression, and other magnetohydrodynamic processes occur similar to those in conventional laser-produced plasmas.[43] Thus, these processes make the system more sensitive to even small changes in the intensity of the focused laser pulse, leading to larger changes in ion and electron emission.

When detecting ion currents, a more pronounced fluctuation is observed between shots, both in the number of ions produced and, in their acceleration, as shown in Fig. 3. Figure 3(a) presents a set of selected detector signals that display fluctuations in ion emission introduced by nonlinearities that may be started by the 6.8% fluctuations in the laser energy (0.350 ± 0.024 mJ). Here, the Cu ion energy corresponding to the maximum signal at $t_{peak}$ fluctuates between 330 keV (shot No. 406, $t_{peak}$ = 0.92 $\mu$s, red line) and 27 keV (shot No. 409, $t_{peak}$ = 3.2 $\mu$s, black line). Figure 3(b) shows a sequence of 110 EM detector signals recorded during a run, highlighting the variation in ion emission between individual shots.

Throughout this paper, specific XFEL pulses are selected for which ion emission analysis is performed. Interaction fluctuations thus allow us to gain broader insight into possible ways of accelerating charged particles. In general, there are several factors causing large interaction fluctuations, like those observed in experiments with conventional lasers. Although the shot-to-shot reproducibility

22 May 2026 09:11:48


© Author(s) 2026

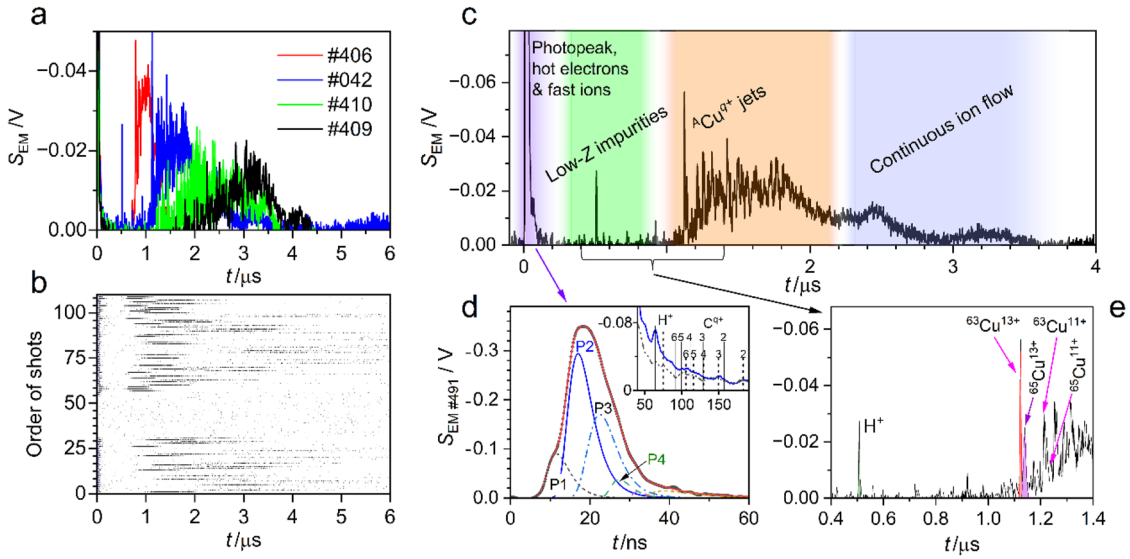


**FIG. 3.** (a) Selected EM signals showing characteristic fluctuations from shot to shot performed under the same experimental conditions. (b) Shot-to-shot fluctuation displayed on the front picture of all TOF signals registered during the run. (c) TOF spectrum associated with shot No. 042. (d) Partitioning of the observed hot-electron and fast-ion peak (No. 491) into partial peaks by fitting the signal function $S_{SMB}(t)$ corresponding to the shifted Maxwell–Boltzmann distribution (see peaks P2 and P3) and the pulse peak function modified by the power term $S_{PF}(t)$ (see peaks P1 and P4). The inset shows details of two TOF spectra (No. 442 and No. 474) displaying the hot electron peak and two peaks induced by $H^+$ ions with energies of 1.08 MeV and 750 keV accompanied by the respective $C^{q+}$ ion groups. (e) Detail of TOF spectrum associated with shot No. 042, providing direct experimental evidence of ion separation in laser-produced plasmas.

is not a primary target of basic research, commercial laser applications such as laser-induced breakdown spectroscopy (LIBS) are trying to address this problem.[44,45] The shot-to-shot reproducibility of detected signals is affected by several factors, which have not yet been fully elucidated. These may include for example, the stability of the laser pulse and the structural heterogeneity of the sample. The extreme nature of the plasma is attributed to the variability of plasma formation and its expansion into vacuum in individual shots. Using experimental data that comprise an averaged set to shrink the influence of fluctuations observed at the individual shot level can be a source of misinterpretations.

### B. Structure of time-of-flight spectra

The beginning of the time-of-flight (TOF) spectrum is related to the first peak (commonly called the photopeak), which is induced by XFEL photons scattered from the target foil. These photons are captured by the EM detector with a delay equal to the photon TOF from the target to the detector. Immediately after the photopeak, other peaks may follow, which are formed by fast (hot) electrons, followed by fast ions of light elements (e.g., hydrogen and carbon) that are part of the impurities on the target surface. Figure 3(c) shows the structure of the EM detector signal, which is formed by a cluster of peaks composed of a photopeak and a group of fast particles such as hot electrons and fast ions [together forming the "HEFI" peak, shown in detail in Fig. 3(d)], followed by a group of low-$Z$ impurities, $^{A}Cu^{q+}$ jets [a detail of which is shown in Fig. 3(e)], and a continuous ion flow. The slower Cu ions arriving at the detector with a delay of several hundred nanoseconds first induce a line spectrum from ≈0.5 to ≈1.8 $\mu$s, and then a continuous profile from ≈1.8 to ≈3.6 $\mu$s. The multiple time scales present in the TOF data are discussed sequentially in the following subsections. In our experiment, the contribution of the scattered laser photons is very weak, the beginning of the detector signal is dominated by the HEFI peak. An example of two HEFI peaks, No. 491 and No. 493, is shown in Fig. 3(d). The HEFI peak (No. 491) can be decomposed into subpeaks by fitting the signal function $S_{SMB}(t)$ corresponding to the shifted Maxwell-Boltzmann distribution (see peaks P2 and P3), and the pulse function of the peak modified by the power term $S_{PF}(t)$, revealing peaks P1 and P4. The inset of Fig. 3(d) shows the details of two TOF spectra (No. 442 and No. 474) displaying a high photo-HEFI peak and two $H^+$ ion peaks occurring at 0.064 and 0.075 $\mu$s with corresponding accelerating voltages of 1.08 and 0.75 MV, respectively, and accompanied by the respective $C^{q+}$ ion groups. Figure 3(d) shows a detail of the TOF spectrum associated with shot No. 042, providing direct experimental evidence of ion separation in laser-produced plasmas. The sharp peak of $H^+$ ions arising at ≈0.51 $\mu$s is well separated from the double peak formed by $^{63}$Cu and $^{65}$Cu isotopes with a charge state of 13. This pair of isotopes is followed by other ions having a lower charge state.

The internal structure of this HEFI peak was revealed using the $S_{SMB}(t)$ and $S_{PF}(t)$ functions fitted to the detector signal $S_{EM}(t)$. When the interaction of the laser with matter creates a statistical ensemble of electrons and ions in thermal equilibrium, they may exhibit a shifted Maxwell–Boltzmann velocity distribution, because in general the expansion may not be of thermal origin only, but may be affected by processes that impart velocity to the plasma plume in a particular direction. The velocity distribution system in the centroidal coordinate system then takes the form

22 May 2026 09:11:48


© Author(s) 2026

$$f(\boldsymbol{v})\ \mathrm{d}\boldsymbol{v} = \left(\frac{m}{2\pi kT}\right)^{2/3} \exp\left[-\frac{m}{2kT}(\boldsymbol{v}-\boldsymbol{u}_{\mathrm{cm}})^2\right]\mathrm{d}\boldsymbol{v}, \tag{2}$$

where $m$ is the particle mass, $k$ is the Boltzmann constant, $T$ is the thermodynamic temperature, and $u_{\mathrm{cm}}$ is the stream velocity (center-of-mass velocity). This is introduced to account for the plasma motion in the $z$ direction, namely, along the target normal. The origin of this velocity can be ascribed, in general, to the pressure gradient, various electrical driving forces and gradients of voltages, such as target normal sheath acceleration, skin-layer ponderomotive acceleration, and the DL effect. Charge separation in the nonequilibrium plasma generates an electric field, which results in a gain in ion energy due to Coulomb acceleration. The corresponding contribution to the total stream velocity, termed the Coulomb velocity by Torrisi *et al.*,[46] is related to the accelerating voltage $U$ by

$$u_{\mathrm{cm}} = \sqrt{2qeU/m}\ . \tag{3}$$

The detector response to the arrival of a statistical ensemble of particles exhibiting the shifted Maxwell–Boltzmann distribution in Eq. (2) can be expressed as

$$S_{\mathrm{SMB}}(t) = a_0 t^{-4} \exp\left[-\frac{m}{2kT}\left(\frac{L}{t}-u_{\mathrm{cm}}\right)^2\right], \tag{4}$$

where $a_0$ is the amplitude and $L$ is the distance of the detector from the target. This function can be applied to the expansion of nonrelativistic particles whose charge is frozen, i.e., without three-body and radiative recombination. The position $t_{\mathrm{peak}}$ of the maximum signal $S_{\mathrm{peak}}$ can be derived from Eq. (4) as follows:

$$t_{\mathrm{peak}} = \frac{L}{v_{\mathrm{peak}}} = \frac{L}{\sqrt{1/2m}\left(\sqrt{10kT+E_{\mathrm{cm}}}+\sqrt{E_{\mathrm{cm}}}\right)}, \tag{5}$$

where $E_{\mathrm{cm}} = \frac{1}{2}mu_{\mathrm{cm}}^2$ is the center-of-mass kinetic energy.

Analysis of HEFI peaks showed that a reasonable fit of the sum of partial signal functions $\sum_p S^p(t)$ to the recorded signal cannot be achieved by fitting only a combination of signal functions given by Eq. (4), i.e., $\sum_p S^p_{\mathrm{SMB}}(t)$, but that it is necessary to combine the $S_{\mathrm{SMB}}$ signal functions with the pulse peak function modified by the power term provided by PeakFit software (Systat, v. 4.12):

$$S_{\mathrm{PF}}(t) = a_0 \frac{\exp\left(\frac{-t-a_1}{a_2}\right)\left[1-\exp\left(\frac{-t-a_1}{a_2}\right)\right]^{a_3}}{a_3^{a_3}\,(a_3+1)^{-a_3-1}}, \tag{6}$$

where $a_0$ is the amplitude, $a_1$ is the pulse initiation (center), $a_2$ is the width, and $a_3$ is the shape. It should be noted that fitting Eq. (6) to the detector signal primarily reveals the amplitude of the current of detected particles. The method of uncovering hidden peaks forming the experimentally observed HEFI peak is based on fitting the sum of functions $\sum_p S^p_{\mathrm{SMB}}(t) + \sum_n S^n_{\mathrm{PF}}(t)$ to the detector signal $S_{\mathrm{EM}}(t)$.

### C. Electrons escaped from plasma

The electrons contribute to the HEFI peak within the spectrum. Figure 3(d) shows that a combination of both types of signal functions $S_{\mathrm{SMB}}$ and $S_{\mathrm{PF}}$ allows the detection of dominant partial peaks P1 to P4. The other two peaks matching the tail of the HEFI peak are not labeled, because their origin cannot be reliably determined. The total number of fitted parameters, including the baseline parameters, was 26. Peaks P2 and P3, which were revealed using the $S_{\mathrm{SMB}}$ function from Eq. (4), provide information about both the current amplitude and $T$ and $u_{\mathrm{cm}}$ of the corresponding particles. The peaks P1 and P4 of the fitted $S_{\mathrm{PF}}$ function indicate the amplitude and velocity of the corresponding groups of particles. The first peak, P1, has a maximum of about 10 ns relative to the incident scattered radiation of the XFEL pulse, which corresponds to the peak energy of ≈11 keV (No. 491). Note that this energy is higher than the XFEL photon energy, appearing to arise from the tail of the electron energy distribution formed in the Cu plasma. The second and third electron bursts are represented by peaks P2 and P3, which were revealed by fitting the $S_{\mathrm{SMB}}$ signal functions. The fitted $E_{\mathrm{peak}}$, $T_{\mathrm{e}}$, and $E_{\mathrm{cm}}$ values of peaks P1, P2, and P3 are summarized in Table I for shots No. 491 and No. 493. Experimental values of $T_{\mathrm{e}}$ obtained from shots No. 491 and No. 493 correspond to the value determined by the theoretical simulations presented in Sec. III, with measured values smaller than the value $T_{\mathrm{e}} \approx 1$ keV calculated for electrons produced inside the irradiated target, as shown in Fig. 1(b).

The presented analysis of the HEFI peaks in Fig. 3(d) and Table I reveals several phenomena. The first of these is the cascade emission of bursts of electrons arriving at the detector at different times. Since the runaway electrons must overcome the electric field created by the electric DL of the plasma, peaks P1, P2, and P3 indicate that it is necessary to deal with the electric fields inside the plasma surfaces, which no longer exhibit static but rather dynamic properties.

The second and third electron bursts, represented by peaks P2 and P3, reveal that the respective electron groups have undergone energy redistribution expressed by different $T_{\mathrm{e}}$ values. The nonzero center-of-mass energy of the electron groups P1 and P2, $E_{\mathrm{cm}} \geq 3$–8 keV, suggests the emergence of an electric field that accelerated the expansion of these electrons by giving them an additional velocity $u_{\mathrm{cm}}$ [see Eq. (3)]. These electric fields could arise because of collective molecular dynamics. However, the PBC simulations used in Sec. III A cannot inherently describe the ejection of surface particles. These electric fields are not static, but dynamic. The runaway electrons forming peaks P1, P2, and P3 should accelerate light impurity ions from the target surface, which impinge on the detector after ~25 ns and later [see P4 in Fig. 3(d)]. Since it is difficult to identify the mass and charge state of these charged particles in this case, Table I does not list the parameters of peak P4 or of others that are not identified. In conclusion, the number of fitted partial peaks is therefore limited not only by the number of electron

**TABLE I.** Fitted values of $E_{\mathrm{peak}}$, $T_{\mathrm{e}}$, and $E_{\mathrm{cm}}$ for the partial peaks P1, P2, and P3 formed by electrons displayed in Fig. 3(d). Peak P1 was revealed using the $S_{\mathrm{PF}}$ function and peaks P2 and P3 using the $S_{\mathrm{SMB}}$ function fitted to the HEFI peak of the EM detector signal for shots No. 491 and No. 493.

| | Shot No. 491 | | | Shot No. 493 | | |
|---|---|---|---|---|---|---|
| Peak | P1 | P2 | P3 | P1 | P2 | P3 |
| $E_{\mathrm{peak}}$ (keV) | 11 | 6.4 | 4.1 | 14 | 8.5 | 5.8 |
| $T_{\mathrm{e}}$ (eV) | ··· | 230 | 360 | ··· | 70 | 210 |
| $E_{\mathrm{cm}}$ (keV) | ··· | 5.6 | 2.8 | ··· | 8.2 | 5 |

22 May 2026 09:11:48


© Author(s) 2026

bursts that occurred by the plasma expansion, but also, for example, by the number of inflection points that are detectable on the HEFI peak envelope and used to fit SMB and PF amplitude models. Although the number of partial electron pulses can be greater than three, their total number is difficult to determine using this method. In the case of fast ions originating from light impurities, which co-form the HEFI peak, the analysis is simpler, since they are mainly hydrogen and carbon ions, i.e., there is a maximum of seven possible partial peaks, as will be shown in Sec. IV D. The expansion of these ions is of course slower than that of electrons.

### D. Fast $H^+$ and $C^{q+}$ ions in HEFI peak

As mentioned above, other peaks appearing at the time of arrival typical for the HEFI peak can also be formed by the detector's response to the capture of fast ions originating from impurities absorbed on the target surface. Local maxima in an HEFI peak or local minima within smoothed second-derivative data are clear indications of these additional species. Shots No. 442 and No. 474 met this condition for revealing hidden peaks corresponding to the fast impurity ions within the HEFI peak. The inset of Fig. 3(d) shows details of these HEFI peaks, with two subpeaks at 0.064 and 0.075 $\mu$s, analysis of which reveals that they were induced by $H^+$ ions moving with kinetic energies of 1.08 MeV and 750 keV, respectively. They are accompanied by groups of $C^{q+}$ ions. Comparison of different TOF spectra allows us to distinguish individual groups of $H^+$ and $C^{q+}$ ions in the descending part of the photo-HEFI peak. Each of the two spectra was analyzed in a range from 0.05 to 0.18 $\mu$s by fitting a series of lines corresponding to TOFs of $H^+$ and $C^{q+}$ accelerated by the same voltage, where $H^+$ ions are faster than $C^{q+}$ ions by a factor of $\sqrt{12/q}$. The corresponding TOF of $C^{q+}$ ion is therefore

$$\mathrm{TOF}_{C^{q+}} = \mathrm{TOF}_{H^+} \times \sqrt{12/q}. \tag{7}$$

Another peak of very low amplitude can be identified at 0.05 $\mu$s, which could be attributed to ≈1.8 MeV $H^+$ ions. The sequential appearance of these peaks in the TOF spectrum suggests that the $H^+$ and $C^{q+}$ ions are accelerated by the same electric field as a compact ensemble of ions.

### E. Bursts of ionized $^{63}$Cu and $^{65}$Cu isotopes

Although Figs. 3(a) and 3(b) attract particular attention because of the large fluctuations in the ion currents, they also reveal another important phenomenon, namely, the nonthermal evolution of the Cu plasma produced by the XFEL beam, as is further indicated by the narrow ion peaks shown in Fig. 3(e). These narrow peaks occur in the detector signal represented by Eq. (4) if $kT \ll E_{\mathrm{cm}}$, and require a modification of the analysis used in the previous case of HEFI spectra to focus instead on finding correlations between the positions of individual peaks on a time scale determined by their center-of-mass velocities, $t_{\mathrm{peak}} = L/u_{\mathrm{cm}}$, as follows from Eq. (5). Since fitting Eq. (4) to the narrow peaks confirms that $kT \ll E_{\mathrm{cm}}$, we can assume that these ions were accelerated by the electric field.

A detailed analysis of the experimentally observed TOF peaks is based on determining the charge state $q$ and the ion kinetic energy $E_q$ represented by the accelerating voltage $U$ corresponding to $t_{\mathrm{peak}}$ of a given peak, according to the relationship

$$E_q = \frac{1}{2}M\left(\frac{L}{\mathrm{TOF}_q}\right)^2 = eUq, \tag{8}$$

where $M$ is the mass of the isotope.

All the $H^+$ and $Cu^{q+}$ ion peaks mentioned above are very narrow, despite having covered $L = 92$ cm. Since their FWHM correlates with the rise and fall times of the detector used, this implies that their velocity distribution is very narrow and their expansion into vacuum is determined primarily by the center-of-mass velocity. The number of $H^+$ ions inducing this peak can be estimated considering the EM gain and amplitude, amounting to only a few thousand ions. With $\mathrm{TOF}_{H^+}$ available, it is possible to determine the kinetic energy of these ions and thus the corresponding acceleration voltage as $U \approx 17$ kV. Assuming this voltage also accelerated the Cu ions forming the above-mentioned double peak, then we can calculate their charge state as $q = 13$. It is also noted that the $H^+$ ions detected in shot No. 042 were practically eliminated from the surface layer of the target by ablating it in high vacuum, and therefore their occurrence in later shots is negligible. It is important to note that these ions were accelerated by a much lower voltage than ions of impurities expanding in the HEFI peak, which were accelerated by a voltage of up to 1 MV.

Suppose that isotopes $^{63}$Cu and $^{65}$Cu flying together as a pair have the same charge state $q$ and are accelerated by a voltage. Then, the ratio of the flight times of $^{63}Cu^{q+}$ and $^{65}Cu^{q+}$ must be equal to the square root of the ratio of their atomic numbers, i.e., $\sqrt{(63/65)} \approx 0.9845$. In this way, the two isotope pairs $^{63}Cu^{13+}/^{65}Cu^{13+}$ and $^{63}Cu^{11+}/^{65}Cu^{11+}$ shown in Fig. 3(d) were identified. The ratio of their measured TOFs is ≈ 0.9866. The deviation of the measured value from the expected value is ≈ 0.2%. The charge states $q_m$ and $q_n$ of adjacent isotope pairs accelerated by the same voltage can also be determined by comparing their TOFs using the ratio $\mathrm{TOF}_{q_m}/\mathrm{TOF}_{q_n} = \sqrt{q_m/q_n}$.

### F. Cascade bursts of Cu ions

In Sec. IV C, it was stated that electrons co-forming the HEFI peak can be divided into three groups that gradually escape from the laser-produced plasma. The peak structure of ionized copper isotopes is not found to correspond to the acceleration of all ions by a fixed voltage, but one that varies over the spatiotemporal scales of their release. It is evident that plasma bursts are related not only to the fastest ionized species, but also to slow species, which are accelerated by a voltage that has dropped from MV values to several kV, as shown in Fig. 4.

The analysis based on Eq. (8) allows a distinction to be made between two ion groups of isotopes $^{63}Cu^{q+}$ and $^{65}Cu^{q+}$ accelerated by different voltages, as shown in Fig. 4. The values of $q$ and $U$, as given in Eq. (8), were determined by matching bi-Gaussian functions to the selected TOF spectrum, considering that $\mathrm{TOF}_{^{63}\mathrm{Cu}}/\mathrm{TOF}_{^{65}\mathrm{Cu}} = \sqrt{63/65}$ holds for each charge state $q$ and $\mathrm{TOF}_{q+1}/\mathrm{TOF}_q = \sqrt{qU_q/[(q+1)U_{q+1}]}$ for each isotope. Keeping these relationships, the matching of bi-Gaussian functions and selected peaks gives three groups of Cu ions with charge state $q$ from 22 to 23, which have kinetic energies corresponding to an accelerating voltage of ≈9.2 kV, and four groups with $q$ from 20 to 23, which have $U \approx 8.5$ kV. Although these two groups of ions do not fully represent all the ions making up this spectrum, others can be identified using the same procedure.

22 May 2026 09:11:48


© Author(s) 2026

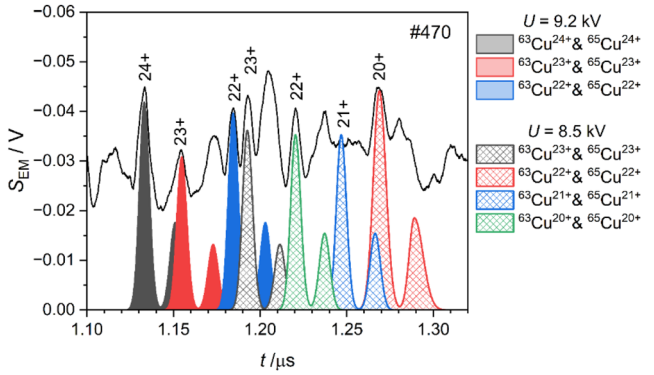


**FIG. 4.** Detail of the TOF spectra of ionized $^{63}$Cu and $^{65}$Cu isotopes produced by shot No. 470 and two sets of numerically simulated double peaks of $^{63}Cu^{q+}$ and $^{65}Cu^{q+}$ ions accelerated at voltages of 8.5 kV (cross-hatched areas) and 9.2 kV (filled areas), respectively.

The calculated values of the ion accelerating voltage provide information about the oscillation of a DL structure, which is manifested by a change in the magnitude of $U$. Figure 4 shows that $^{63}Cu^{23+}$ ions accelerated by 8.54 kV arrived at the detector ≈38 ns after $^{63}Cu^{23+}$ ions accelerated by 9.18 kV. To remove the $q$ and $M$ dependences of the TOF of Cu ions [see Eq. (7)], the TOF of protons, which are accelerated by the same voltage as the Cu ions and move behind them, can be considered. From the obtained voltage values, the time delay $\Delta t_L$ between corresponding proton peaks at the ion detector can be calculated. This delay can be transformed to the proximity of the target using the velocity $v = L/t$ as a similarity parameter:

$$\Delta t_{\mathrm{DL}} = \Delta t_L (L_{\mathrm{DL}}/L), \tag{9}$$

where $\Delta t_{\mathrm{DL}}$ is the estimated delay in the emission of ions at $L_{\mathrm{DL}} = 1$ $\mu$m, which is the distance corresponding to the estimated plasma dimension related to the diameter of the measured XFEL beam focus. The delay value $\Delta t_{\mathrm{DL}}$ can be interpreted as the time of creation of the subsequent DL-generating voltage $U(t + \Delta t_{\mathrm{DL}})$, but less than the $U(t)$ of the previous DL. The estimated value for the two ion groups shown in Fig. 4 is $\Delta t_{\mathrm{DL}} \approx 40$ fs. The experiment shows that each group of ions emitted at later times was accelerated by a smaller voltage.

The TOF analysis of the individual peaks in Fig. 4 confirms that there are a series of jumps and dips created by the DLs at the periphery of the expanding laser-produced plasma, as theoretically indicated by Eliezer and Hora.[40] In our experiment, the time sequence of these DLs is in the frequency region of 10 THz, as revealed by the transition from the meter to the micrometer scale of the location of the ion current measurement. Although this is only an estimate, $\Delta t_{\mathrm{DL}}$ is one of the key parameters of the dynamic electric fields associated with the DL in the process of particle acceleration to high energies. The repetition of ion jets, which has also been observed experimentally during the interaction of a nanosecond laser pulse with a solid target,[47] suggests the occurrence of hydrodynamic oscillations of the DL with a period of tens of femtoseconds or longer.[40] We can expect that application of this method to the analysis of all distinguishable ion jets will allow us to obtain the full spectrum of DL oscillations. It is evident that the electric fields and the corresponding potentials that occur inside the plasma sheath and accelerate the ions are not static but dynamic,[40–42] although this approximation does not provide information about when these oscillations occur after the ultrafast laser pulse interaction with matter.

## G. Collective behavior of ions

The expansion of ionized Cu isotopes into vacuum as temporally isolated jets is observable up to ~1.8 $\mu$s, after which the individual jets begin to overlap and the ion stream becomes continuous, as shown in Fig. 3(c). A standard feature of jet emission is that the amplitude of the ion current peaks increases until a first maximum, in the case of the burst shown in Fig. 3(c) at a time of ~1.3 $\mu$s. Further maxima may then appear. However, a time-resolved ion current density $j(t)$ measured at a certain distance $L$ from the target can be transformed into a distance-resolved ion charge density $\rho_i(z)$ at a selected time $\tau$.[22] This transformation is derived from a similarity relation for the ion current density measured at different distances from the target, namely, $j(z, \tau)z^3 = j(L, t)L^3$, where the velocity $v = z/\tau = L/t$ is the similarity parameter, which follows from the assumption of conservation of the charge carried by ions far from the target, whose charge density decreases as $L^{-2}$. Considering the relationship $z = L\tau/t$, which is applicable to $v$, the spatial distribution of the ion charge density, i.e., the distance-of-flight (DOF) spectrum, can then be revealed using the relationship[22]

$$\rho_i(z, \tau) = j(z)\tau L^3/z^4. \tag{10}$$

An example of the transformation of the TOF spectrum of the ion current represented by the $S_{\mathrm{EM}}$ detector signal into the DOF spectrum of the ion charge density is shown in Fig. 5. The detector signal is shown in the inset.

The calculated $\rho_i(z)$ shows that 1 $\mu$s after the laser interaction, the distance between the ion peaks varies in the range of millimeters to centimeters. Analysis reveals that the fastest ions occurring farthest from the target (>84 cm) had $q > 20$ and were accelerated by $U > 10$ kV. The corresponding part of the $S_{\mathrm{EM}}$ signal is highlighted in green in the inset of Fig. 5. While the fastest ions are grouped at 90 cm from the target into a bunch about 15 cm wide, the slower Cu ions occupying the space between 57 and 83 cm form a group whose mean charge density profile appears as $\rho(z) = \rho_0 e^{-z/\zeta}$, as shown by the red line in Fig. 5. Expressing the charge density of ions as the product of the ion density and the mean charge $e\bar{q}$ of ions, i.e., $\rho_i(z, t)/(e\bar{q}) = n_i(z, t)$, where $\bar{q}$ is the mean value of the charge, the density profile $\rho_0 e^{-z/\zeta}/(e\bar{q})$ of ions can be written in the form[48]

$$n_i(z, t) = n_0 e^{-1-z/(tc_s)}. \tag{11}$$

Substituting $t = \tau$ gives

$$n_i(z, \tau) = \frac{n_0}{e} e^{-z/(\tau c_s)}, \tag{12}$$

where $\tau$ is the above-mentioned chosen time, $c_s = \sqrt{\bar{q}\gamma kT_e/M_i}$ is the ion sound velocity (where $\gamma$ is normally taken to be unity), and $z/\tau$ the velocity of ions located at a distance $z$ from the target at time $\tau$. The exponential decrease in the ion density profile, indicated by the

22 May 2026 09:11:48


© Author(s) 2026

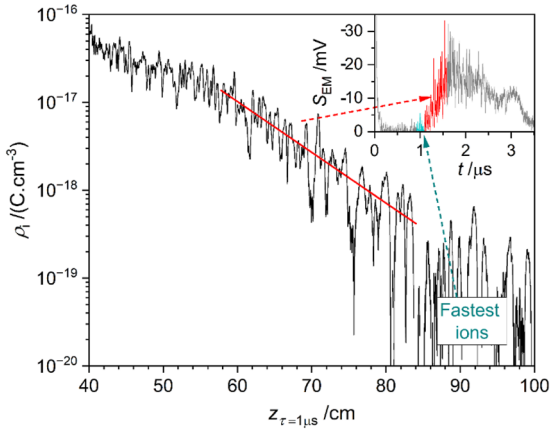


**FIG. 5.** Distance-of-flight (DOF) spectrum of ion density obtained by transformation of the signal of the 119EM electron multiplier induced by ions produced by interaction of the European XFEL beam of 9.3 keV photons with a Cu foil target (shot No. 478) for a time of 1 $\mu$s elapsed since the laser–target interaction. The red line shows the fit of Eq. (12) to the DOF spectrum to estimate the value of the ion sound velocity $c_s$. The inset shows the source TOF spectrum detected at 92 cm from the target. The fastest $Cu^{q+}$ ions ($q > 20$) are accelerated by a voltage larger than 10 kV. The green and red arrows point to the corresponding parts of the DOF and TOF spectra.

red line in Fig. 5, can then be identified with the exponent in Eq. (12). The fitted value of $\zeta = \tau c_s$ allows us to calculate the value of $c_s = 7.5 \times 10^6$ cm/s. Since the estimated mean charge state value of these ions accelerated by a voltage of ≈7.8 kV is $\bar{q} = 18$, the corresponding electron temperature $kT_e \approx 200$ eV. This result is consistent with the result of the analysis of electrons in Sec. IV C. The corresponding part of the $S_{EM}$ signal is highlighted in red in the inset of Fig. 5. This reveals that these ions form the leading edge of the current of Cu ions ($S_{EM}$ signal). It is apparent that the group of ions forming the $S_{EM}$ leading edge contains subgroups of ions that have been characterized in the earlier discussion and presented in Figs. 3(e), 4, and 5. Hot electrons with $kT_e \approx 200$ keV, which escaped from the plasma first, control the density profile of the fastest Cu ions, although they were accelerated in a few DLs.

It can be surmised that owing to the distance from the target, the electron and ion currents were measured in regions where recombination processes in the expanding laser-produced plasma had slowed down rapidly, and the charge states of the ions had become "frozen." The ion charge density profile calculated from the time-resolved currents of charged particles emitted by the target shows that only a part of the density profile exhibits an exponential decay with increasing distance. This decay, characterized by the exponential decay function $e^{-v/c_s}$, does not change with time $\tau$, because the choice of $\tau$ does not affect the velocity $v$ of the expanding ions.

## V. CONCLUSIONS

The irradiation of solid foil targets by ultrashort, hard X-ray FEL radiation of 9.3 keV photon energy delivered to the High Energy Density (HED) Scientific Instrument at the European XFEL facility resulted in the emission of highly charged Cu ions. Ions were produced with a fluence of ≈280 kJ/cm$^2$ delivered onto a 3 $\mu$m Cu foil in pulses of 25 fs duration. Numerical simulations of the early stage of plasma formation in bulk copper using the XMDYN tool demonstrated that under the irradiation conditions of the experiment, copper ions with charge beyond 20 were formed. Furthermore, within 100 fs after the pulse, the electron kinetic temperature approached 1 keV.

As the number of charged species emitted into vacuum is small, an open electron multiplier with a gain of $5 \times 10^5$ was used for their registration. Ion emission in the backward direction, i.e., from the front side of the foil, occurred, with negligible ion emission from the rear surface, mostly below the detection threshold. Owing to the low number of emitted electrons and ions, clusters of both electrons and separated jets of highly ionized Cu isotopes were observed, with large shot-to-shot variations. Using the shifted Maxwell–Boltzmann distribution function, the temperature of the electrons and the kinetic energy of their center of mass were determined for multiple jets, with a maximum measured electron temperature of 360 eV, which is lower than the calculated value for the plasma produced during the X-ray laser pulse interaction. However, the identified kinetic energy of the center of mass could also be affected by a Coulomb explosion.

The correlation between the kinetic energies of individual ion peaks revealed the accelerating voltage experienced by the ions, coming from a DL, allowing identification of both $^{63}$Cu and $^{65}$Cu isotopes, as well as their charge state. Analysis of multiple jets of ion species arriving at the detector showed that the voltage, reaching several keV, oscillated and gradually decreased during the plasma quenching process. This indicates complex motion in the DL separating the plasma from the vacuum as the fastest electrons escaped from the plasma. Although the ion emission initially occurred in the form of jets separated in time, surprisingly, this plasma also exhibited continuum properties that can be characterized by the ion sound velocity and the corresponding electron temperature, which in this case was ≈200 eV, with a group of fast ions whose $\bar{q}$ value calculated for a time of 100 fs after the interaction correlates with the experimentally evaluated one.

The work presented here shows that ultrashort X-ray pulses delivered by an XFEL can yield rich experimental data that help unravel the expansion of plasma into vacuum. These observations provide information on the surface effects of dense plasmas, missing from the available collisional radiative codebase, but of importance for laser plasma experiments, which commonly make use of very thin foils of the order of the optical skin depth.

## ACKNOWLEDGMENTS

The research presented in this paper was supported by the Czech Republic's Ministry of Education, Youth and Sports (Project No. LM2023068). We acknowledge the European XFEL in Schenefeld, Germany, for provision of X-ray free electron laser beam time at the Scientific Instrument HED (High Energy Density Science) and would like to thank the staff for their assistance. The authors are indebted to the Helmholtz International Beamline for Extreme Fields (HIBEF) user consortium for the provision of instrumentation and staff that enabled this experiment. Z.J. and R.S.

22 May 2026 09:11:48


© Author(s) 2026

acknowledge support from DESY (Hamburg, Germany), a member of the Helmholtz Association HGF.

## AUTHOR DECLARATIONS

### Conflict of Interest

The authors have no conflicts to disclose.

### Author Contributions

**T. Burian**: Conceptualization (equal); Investigation (equal); Methodology (equal); Resources (equal); Supervision (equal); Validation (equal). **J. Krása**: Conceptualization (equal); Formal analysis (equal); Methodology (equal); Resources (equal); Writing – original draft (equal). **M. Šmíd**: Data curation (equal); Investigation (equal); Project administration (equal); Supervision (equal); Writing – review & editing (equal). **M. Krupka**: Data curation (equal); Formal analysis (equal); Investigation (equal). **M. Stránský**: Data curation (equal); Formal analysis (equal). **Z. Jurek**: Data curation (equal); Formal analysis (equal); Writing – review & editing (equal). **R. Santra**: Data curation (equal); Formal analysis (equal); Writing – review & editing (equal). **J. Chalupský**: Data curation (equal); Formal analysis (equal); Investigation (equal); Writing – review & editing (equal). **L. Vyšín**: Data curation (equal); Investigation (equal). **A. Hornyová**: Data curation (equal); Investigation (equal). **J. Bulička**: Data curation (equal); Investigation (equal). **Š. Jelínek**: Data curation (equal); Formal analysis (equal); Investigation (equal). **M. Kozlová**: Data curation (equal); Investigation (equal). **M. Mašek**: Data curation (equal); Formal analysis (equal). **O. Humphries**: Data curation (equal); Investigation (equal); Writing – review & editing (equal). **C. Baehtz**: Data curation (equal); Investigation (equal). **V. Bouffetier**: Data curation (equal); Investigation (equal). **E. Brambrink**: Data curation (equal); Investigation (equal). **V. Cerantola**: Data curation (equal); Investigation (equal). **T. E. Cowan**: Project administration (equal); Resources (equal); Supervision (equal). **V. Hájková**: Data curation (equal); Formal analysis (equal); Investigation (equal). **J. Kaa**: Data curation (equal); Investigation (equal). **Z. Konôpková**: Data curation (equal); Investigation (equal). **M. Makita**: Data curation (equal); Investigation (equal). **X. Pan**: Data curation (equal); Investigation (equal). **T. R. Preston**: Data curation (equal); Investigation (equal). **J.-P. Schwinkendorf**: Data curation (equal); Investigation (equal). **A. Schropp**: Data curation (equal); Investigation (equal). **R. Štefaníková**: Data curation (equal); Investigation (equal). **W. Wang**: Data curation (equal); Investigation (equal). **U. Zastrau**: Data curation (equal); Investigation (equal). **K. Falk**: Conceptualization (equal); Methodology (equal); Project administration (equal). **L. Juha**: Conceptualization (equal); Funding acquisition (equal); Investigation (equal); Methodology (equal); Project administration (equal); Resources (equal); Supervision (equal); Writing – review & editing (equal).

## DATA AVAILABILITY

The data that support the findings of this study are openly available upon reasonable request at https://in.xfel.eu/metadata/doi/10.22003/XFEL.EU-DATA-002806-00.

## REFERENCES

[1] D. W. Koopman, "Ion emission from laser-produced plasmas," Phys. Fluids **10**, 2091 (1967).
[2] S. Ter-Avetisyan, L. Romagnani, M. Borghesi, M. Schnürer, and P. V. Nickles, "Ion diagnostics for laser plasma experiments," Nucl. Instrum. Methods Phys. Res., Sect. A **623**, 709 (2010).
[3] M. G. Johnson, "Charged particle diagnostics for inertial confinement fusion and high-energy-density physics experiments," Rev. Sci. Instrum. **94**, 021104 (2023).
[4] B. Sharkov, "Laser ion sources," in *The Physics and Technology of Ion Sources*, 2nd ed. (Wiley-VCH, 2004), pp. 233–256.
[5] H. Daido, M. Nishiuchi, and A. S. Pirozhkov, "Review of laser-driven ion sources and their applications," Rep. Prog. Phys. **75**, 056401 (2012).
[6] H. Hora, J. Badziak, F. P. Boody, R. Höpfl, K. Jungwirth *et al.*, "Effects of ps and ns laser pulses for giant ion source," Opt. Commun. **207**, 333 (2002).
[7] L. Láska, J. Badziak, F. P. Boody, S. Gammino, K. Jungwirth *et al.*, "Factors influencing parameters of laser ion sources," Laser Part. Beams **25**, 199 (2007).
[8] M. Okamura, "Laser ion source for heavy ion inertial fusion," Matter Radiat. Extremes **3**, 61 (2018).
[9] C. Pagani, E. L. Saldin, E. A. Schneidmiller, and M. V. Yurkov, "Design considerations of 10 kW-scale, extreme ultraviolet SASE FEL for lithography," Nucl. Instrum. Methods Phys. Res., Sect. A **463**, 9 (2001).
[10] G. Dattoli, P. L. Ottaviani, A. Renieri, S. G. Biedron, H. P. Freund *et al.*, "A compact free electron laser device operating in the UV-soft X-ray region," Opt. Commun. **232**, 319 (2004).
[11] J. B. Rosenzweig, N. Majernik, R. R. Robles, G. Andonian, O. Camacho *et al.*, "An ultra-compact x-ray free-electron laser," New J. Phys. **22**, 093067 (2020).
[12] M. Galletti, R. Assmann, M. E. Couprie, M. Ferrario, L. Giannessi *et al.*, "Prospects for free-electron lasers powered by plasma-wakefield-accelerated beams," Nat. Photonics **18**, 780 (2024).
[13] I. Kuznetsov, J. Filevich, F. Dong, M. Woolston, W. Chao *et al.*, "Three-dimensional nanoscale molecular imaging by extreme ultraviolet laser ablation mass spectrometry," Nat. Commun. **6**, 6944 (2015).
[14] D. Bleiner, L. Juha, and D. Qu, "Soft X-ray laser ablation for nano-scale chemical mapping microanalysis," J. Anal. At. Spectrom. **35**, 1051–1070 (2020).
[15] J. Bulička, L. Vyšín, N. Medvedev, V. Hájková, L. Fekete *et al.*, "Damage thresholds revealed by ions emitted from boron nitride and tungsten exposed to energetic photons at high dose rates," J. Nucl. Mater. **616**, 156069 (2025).
[16] L. Vyšín, J. Chalupský, L. A. Rush, L. Fekete, J. Bulička *et al.*, "Behavior of poly(methyl methacrylate) exposed to extreme ultraviolet laser radiation: A relationship between the high-energy photo-decomposition of the polymer and the mass spectra of emitted ions," Polym. Degrad. Stab. **236**, 111298 (2025).
[17] B. Rus, T. Mocek, M. Kozlová, J. Polan, P. Homer *et al.*, "High energy density matter generation using a focused soft-X-ray laser for volumetric heating of thin foils," High Energy Density Phys. **7**, 11 (2011).
[18] D. Riley, *Warm Dense Matter: Laboratory Generation and Diagnosis* (IOP Publishing, 2021).
[19] S. M. Vinko, O. Ciricosta, B.-I. Cho, K. Engelhorn, H.-K. Chung *et al.*, "Creation and diagnosis of solid-density hot-dense matter with an X-ray free-electron laser," Nature **482**, 59 (2012).
[20] R. Sobierajski, J. Krzywinski, A. Andrejczuk, U. Hahn, R. Treusch *et al.*, "Experimental station to study the interaction of intense femtosecond vacuum ultraviolet pulses with matter at TTF1 free electron laser," Rev. Sci. Instrum. **76**, 013909 (2005).
[21] B. Iwan, J. Andreasson, A. Andrejczuk, E. Abreu, M. Bergh *et al.*, "TOF-OFF: A method for determining focal positions in tightly focused free-electron laser experiments by measurement of ejected ions," High Energy Density Phys. **7**, 336 (2011).
[22] J. Krása, T. Burian, V. Hájková, J. Chalupský, Š. Jelínek *et al.*, "Ion emission from warm dense matter produced by irradiation with a soft x-ray free-electron laser," Matter Radiat. Extremes **9**, 016602 (2024).
[23] U. Zastrau, K. Appel, C. Baehtz, O. Baehr, L. Batchelor *et al.*, "The high energy density scientific instrument at the European XFEL," J. Synchrotron Radiat. **28**, 1393 (2021).

22 May 2026 09:11:48


© Author(s) 2026

[24]W. Decking, S. Abeghyan, P. Abramian, A. Abramsky, A. Aguirre *et al.*, "A MHz-repetition-rate hard X-ray free-electron laser driven by a superconducting linear accelerator," Nat. Photonics **14**, 391 (2020).
[25]J. Grűnert, M. P. Carbonell, F. Dietrich, T. Falk, W. Freund *et al.*, "X-ray photon diagnostics at the European XFEL," J. Synchrotron Radiat. **26**, 1422 (2019).
[26]V. Hájková, L. Juha, P. Boháček, T. Burian, J. Chalupský *et al.*, "X-ray laser-induced ablation of lead compounds," Proc. SPIE **8077**, 807718 (2011).
[27]J. Chalupský, J. Krzywinski, L. Juha, V. Hájková, J. Cihelka *et al.*, "Spot size characterization of focused non-Gaussian X-ray laser beams," Opt. Express **18**, 27836 (2010).
[28]J. Krása, M. Pfeifer, M. P. Stockli, U. Lehnert, and D. Fry, "The effect of the first dynode's geometry on the detection efficiency of a 119EM electron multiplier used as a highly charged ion detector," Nucl. Instrum. Methods Phys. Res., Sect. B **152**, 397 (1999).
[29]D. Kraus, T. R. Preston, and U. Zastrau, "Warm dense matter studies with X-ray free-electron lasers," Nat. Rev. Phys. **8**, 27 (2026).
[30]S. M. Vinko, O. Ciricosta, T. R. Preston, D. S. Rackstraw, C. R. D. Brown *et al.*, "Investigation of femtosecond collisional ionization rates in a solid-density aluminium plasma," Nat. Commun. **6**, 6397 (2015).
[31]T. Gawne, T. Campbell, A. Forte, P. Hollebon, G. Perez-Callejo *et al.*, "Investigating mechanisms of state localization in highly ionized dense plasmas," Phys. Rev. E **108**, 035210 (2023).
[32]M. Šmíd, O. S. Humphries, C. Baehtz, V. Bouffetier, E. Brambrink *et al.*, "Plasma screening in mid-charged ions observed by K-shell line emission," Sci. Rep. **16**, 5873 (2026).
[33]Z. Jurek, S.-K. Son, B. Ziaja, and R. Santra, "*XMDYN* and *XATOM*: versatile simulation tools for quantitative modeling of X-ray free-electron laser induced dynamics of matter," J. Appl. Crystallogr. **49**, 1048 (2016).
[34]B. F. Murphy, T. Osipov, Z. Jurek, L. Fang, S.-K. Son *et al.*, "Femtosecond X-ray-induced explosion of $C_{60}$ at extreme intensity," Nat. Commun. **5**, 4281 (2014).
[35]S.-K. Son, L. Young, and R. Santra, "Impact of hollow-atom formation on coherent x-ray scattering at high intensity," Phys. Rev. A **83**, 033402 (2011).
[36]S.-K. Son, L. Budewig, R. Jin, J. J. Bekx, K. Toyota *et al.*, "XATOM – An integrated toolkit for x-ray and atomic physics," in *XRAYPAC* (Deutsches Elektronen-Synchrotron DESY, 2025), Version 2.1.0, GitLab.
[37]L. Inhester, Z. Jurek, S.-K. Son, M. M. Abdullah, and R. Santra, "XRAYPAC – A software package for modelling x-ray-induced dynamics of matter," in *XRAYPAC* (Deutsches Elektronen-Synchrotron DESY, 2025), Version 2.1.0, GitLab.
[38]H. Yoneda, Y. Inubushi, M. Yabashi, T. Katayama, T. Ishikawa *et al.*, "Saturable absorption of intense hard X-rays in iron," Nat. Commun. **5**, 5080 (2014).
[39]K. Toyota, Z. Jurek, S.-K. Son, H. Fukuzawa, K. Ueda *et al.*, "*xcalib*: A focal spot calibrator for intense X-ray free-electron laser pulses based on the charge state distributions of light atoms," J. Synchrotron Radiat. **26**, 1017 (2019).
[40]S. Eliezer and H. Hora, "Dynamic electric fields and double layers in laser-produced plasmas," Fusion Technol. **16**, 419 (1989).
[41]N. Hershkowitz, "Review of recent laboratory double layer experiments," Space Sci. Rev. **41**, 351 (1985).
[42]C. Charles, "A review of recent laboratory double layer experiments," Plasma Sources Sci. Technol. **16**, R1–R25 (2007).
[43]L. Huang, M. Šmíd, L. Yang, O. Humphries, J. Hagemann *et al.*, "Demonstration of full-scale spatiotemporal diagnostics of solid-density plasmas driven by an ultra-short relativistic laser pulse using an X-ray free-electron laser," Matter Radiat. Extremes **11**, 017201 (2026).
[44]A. P. M. Michel, "Review: Applications of single-shot laser-induced breakdown spectroscopy," Spectrochim. Acta, Part B **65**, 185 (2010).
[45]S. Sheta, M. S. Afgan, L. Jiacen, W. Gu, Z. Hou *et al.*, "Insights into enhanced repeatability of femtosecond laser-induced plasmas," ACS Omega **5**, 30425 (2020).
[46]L. Torrisi, L. Andò, S. Gammino, and L. Láska, "Tantalum ions produced by 1064 nm pulsed laser irradiation," J. Appl. Phys. **91**, 4685 (2002).
[47]J. Krása, A. Velyhan, K. Jungwirth, E. Krouský, L. Láska *et al.*, "Repetitive outbursts of fast carbon and fluorine ions from sub-nanosecond laser-produced plasma," Laser Part. Beams **27**, 171 (2009).
[48]V. Tikhonchuk, *Particle Kinetics and Laser-Plasma Interactions* (Cambridge Scholars Publishing, 2023), pp. 65–67.

22 May 2026 09:11:48


© Author(s) 2026